scientific reports

Check for updates

OPEN

The impact of graphene oxide on the magnetic and hyperthermia properties of $CoFe_2O_4$ and $MnFe_2O_4$ ferrites

Wegdan Ramadan[1]✉, Aya Gasser[1], Abdallah Ramadan[1], Marcos Garcia[2], Yohannes Getahun[2] & Ahmed A. El-Gendy[2]✉

$MnFe_2O_4$ and $CoFe_2O_4$ nanoparticles, along with their graphene oxide (GO) composites, were synthesized and characterized for potential use in magnetic hyperthermia applications. $MnFe_2O_4$ and $CoFe_2O_4$ were synthesized through hydrothermal method and characterized using XRD, TEM, Raman, FTIR spectroscopy and VSM to determine their structural, morphological, and magnetic properties. Magnetic measurements revealed superparamagnetic behavior in $MnFe_2O_4$, while $CoFe_2O_4$ exhibited ferromagnetic properties. $MnFe_2O_4$, with soft ferrite characteristics, demonstrated higher magnetization and heating efficiency compared to $CoFe_2O_4$, a hard ferrite with higher magnetic anisotropy. The incorporation of graphene oxide introduced competing effects: while it improved colloidal dispersion and offered a surface platform amenable to bioconjugation and functionalization for targeted drug delivery, it consistently reduced SAR values across both ferrite systems. This reduction is attributed to magnetic phase dilution by the nonmagnetic GO matrix, as well as domain pinning caused by interfacial strain and structural defects, reflecting perturbations to the magnetic microstructure. Enhancing the hyperthermia performance of ferrites may require optimizing more than just saturation magnetization; factors such as the anisotropy constant of the ferrite must be tuned to match the relaxation timescale with the applied field frequency. Hyperthermia experiment demonstrated enhanced heating efficiency (SAR values) for $MnFe_2O_4$, achieving 110 W/g, compared to its GO composite (60 W/g), highlighting the synergistic effects of both Néel and Brownian relaxation mechanisms whose effective relaxation time is better matched to the applied frequency. On the other hand, $CoFe_2O_4$ system operates predominately through Brownian relaxation, as its Néel relaxation is thermally inaccessible under these conditions, resulting in a much lower SAR of 70 W/g. The composite, $CoFe_2O_4$-GO, exhibited lower but comparable SAR values, decreasing from 70 to 60 W/g, consistent with a Brownian-dominated mechanism relatively insensitive to GO-induced magnetic modifications. In this study, we identify some key parameters influencing hyperthermia performance (e.g., particle size, morphology, and magnetic anisotropy) in an effort to present optimized nanoparticles for effective hyperthermia-based cancer treatment.

Nowadays, researchers show more attention and interest in hyperthermia as a therapeutic method that generates suitable heat and is a promising method for cancer treatment[1]. Hyperthermia initiates a localized increase in the order of 5°–7° more than the physiological temperature, i.e. in the range of 41–45 °C. Effective local or regional hyperthermic cancer therapy can be induced by either longer heating durations at temperatures of 41–45 °C or by short duration treatment of cancer cells with higher temperatures, or both[2]. However, hyperthermia alone is not enough to be used as a sole treatment technique for cancer, but rather in a synergistic manner with other techniques like chemotherapy and radiotherapy[3,4]. According to the National Cancer Institute (NCI), there are many ways to induce localized hyperthermia like microwaves, radiofrequency, ultrasound and even light. Traditional hyperthermia techniques using radiofrequency and microwaves have their own limitations; they are invasive and lead to serious side effects. Light is another method of hyperthermia such as it causes photothermal treatment using infra-red radiation, generating heat and inducing the necrosis or apoptosis of cancer cells. Another crucial disadvantage of light is the lack of depth in its penetration into the tissues, thus proving to

[1]Department of Physics, Faculty of Science, Alexandria University, Alexandria 21511, Egypt. [2]Department of Physics, University of Texas at El Paso, El Paso, TX 79968, USA. ✉email: wegdan.ramadan@alexu.edu.eg; aelgendy@utep.edu

be futile for deep tumor therapy. Gold nanoparticles in its different shapes, carbon nano tubes and polymers such as polyaniline[5–9] can be used for photothermal cancer therapy as they can be injected and reach the local tumor area in a targeted manner and can be stimulated via near infra-red laser light to generate heat. Oxides, including magnetic oxides/ferrites, have been used for many different electronic applications and for energy storing[10–14]. On the other hand, magnetic nanoparticles such as ferrites, iron oxide[15,16] and superparamagnetic iron oxide nanoparticles (SPIONs)[17] can be stimulated via alternating magnetic fields or microwaves to generate heat. Such magnetic nanoparticles can generate hyperthermia and increase the surrounding temperature to 41–45 °C. The mechanism of heat dissipation using MNPs involves a delay in the relaxation of the magnetic moments, either due to rotation within the particle (Néel) or due to rotation of the particle itself (Brownian) when an AC magnetic field is applied, in which the magnetic field reversal time is shorter than the magnetic moment relaxation of the nanoparticles[18,19]. When applying an alternating magnetic field (AMF) to magnetic nanoparticles, MNPs, the specific area of the magnetic hysteresis loop, A, corresponds to the dissipated energy used. The power generated by the MNPs known as specific absorption rate (SAR) and the hysteresis loop area, A, are linked by the equation of $\mathbf{SAR} = \boldsymbol{Af}$, where f is the frequency of the applied alternating magnetic field[20,21]. The challenge here is the development of MNPs with high SAR performance to reduce the in vivo ferrofluid dose and minimize the potential side effects that could arise during treatment[22–24]. For medical reasons, humans cannot be exposed to an alternating magnetic field having large intensity nor having large frequency[25]. Typical reported values used for medical purposes are around 100 kHz and 20 mT[26]. Hence, it would be more convenient to resolve the optimization of other important parameters that influence SAR values like the particle size, saturation magnetization, morphology and magnetic anisotropy[27]. Such an optimization process needs a careful analysis of the combined influence of the mentioned parameters. Many precautions must be considered when dealing with hyperthermia such as the fluid containing magnetic nanoparticles are commonly water or saline and nanoparticles must be non-toxic and can work at the physiological pH. Also, MNPs must be tiny enough to be entrapped by cancer cells[28]. Another important parameter that determines the value of the induced heat and reproducibility of the obtained results is MNPs dispersion in solutions. Dispersion is essential to prevent MNPs precipitation and aggregation during the time of carrying out the experiment. In this context, highly dispersible graphene oxide sheets, GO, are used as platform to host and assemble MNPs on top of it. GO has high surface area and is biocompatible and by the functionalization of the MNPs through van der Waal force it is possible to attach MNPs to the GO sheets[29]. Ferrites are a class of ferrimagnetic materials primarily composed of iron oxide, having the general formula MFe_2O_4, where M is divalent metal ions like Mn^{2+}, Fe^{2+}, Co^{+}, Ni^{2+}, Cu^{2+}, Zn^{2+}, Mg^{2+} or Cd^{2+}. Their spinel structure allows for the distribution of cations among tetrahedral and octahedral sublattices, enabling precise tuning of magnetic and hyperthermia properties. The large number of possible combinations make ferrite highly versatile, offering broad relevance in applications that improve quality of life[30]. Engineering their properties involves adding two or more dopants such as divalent metal ions Mn and Zn, rare-earth ions, or other metal oxides to tailor structural, magnetic, and electrical properties. This include increasing coercivity, enhancing magnetization, or reducing power loss for high-frequency applications[31]. Careful optimization of divalent cation substitution, such as Mn within iron ferrite, has shown a remarkable increase of around 181% in specific absorption rate (SAR), reaching 510 kW/kg[32]. This enhancement upon Mn doping is attributed to the elevated saturation magnetization resulting from the appropriate cation distribution within the MNPs. Furthermore, the increase in spin relaxation time with higher Mn concentration also contributes to the increased SAR values as MNPs retain their moments for extended period before relaxing, leading to higher SAR values. Another important application of ferrites, that is widely investigated is photocatalytic wastewater remediation, in which doping can modulate the bandgap of ferrites, thus improving activity under visible light[33–36]. On the other hand, cobalt ferrite ($CoFe_2O_4$) is a particularly compelling material to explore; it is a spinel ferrite known for its outstanding structural and magnetic properties, including high saturation magnetization and robust magneto crystalline anisotropy[37]. Furthermore, its relatively high Curie temperature and robust structural stability up to 600 °C ensure thermal stability under physiological conditions, a critical requirement for the sustained therapeutic use of magnetic nanoparticles[38–40]. However, the biocompatibility and cytotoxicity of $CoFe_2O_4$ and other ferrite nanoparticles are critical concerns for biomedical applications, such as magnetic hyperthermia[41]. Therefore, functionalizing ferrites with materials like chitosan, PEG, graphene, or graphene oxide (GO)[42] is a vital strategy to ensure biological safety, while also enhancing dispersibility in solutions[43].

In this work, $MnFe_2O_4$ and $CoFe_2O_4$ MNPs and their composites with GO were synthesized in one pot hydrothermal reaction. $CoFe_2O_4$ and $MnFe_2O_4$ are both ferrimagnetic compounds but have different magnetic behaviors, $MnFe_2O_4$ being classified as "soft ferrite" and $CoFe_2O_4$ as "hard ferrite" and this is attributed to the different inversion degree characterizing each one of these ferrites. While bulk cobalt ferrite is considered to display the completely inverse spinel structure, with all Co (II) ions exclusively at octahedral lattice sites, bulk $MnFe_2O_4$ adopts an almost normal spinel structure with a low degree of inversion[44,45] corresponding to the formula $(Mn_{0.8}Fe_{0.2})\,[Mn_{0.2}Fe_{1.8}]O_4$. The variation in the magnetic structures and properties will boost variation on other parameters that could benefit applications like hyperthermia. This includes, but not only limited to, magnetic anisotropy, k, magnetic parameters like saturation magnetization, M_s, area of hysteresis loop, A, remnant magnetization, M_r, and superparamagnetic behavior. The choice of manganese ferrite NPs is due to its low toxicity, high stability, easily synthesized and tunable magnetic properties[46]. Many techniques are currently developed and used for the synthesis of MNPs[47–49] which in turn allows engineering of many parameters that are required for the intended applications. Most of the investigations on magnetic nanoparticles have been carried out on spherical shaped nanoparticles, although other shapes (rods, disks, cubes, rhombohedral, or more complex shapes) have also been successfully synthesized. And in many cases mixed morphologies results as a final product that is used and assessed. We show experimentally that the difference in effective surface anisotropy between different NPs geometries leads to substantial differences in magnetic and anisotropy properties. However, the efficiency of hyperthermia as a therapy depends also, and to a large extent, on the MNPs' physical characteristics:

types, sizes and shapes[50]. Some reported values of SAR for cuboid/cubes of 17.6 nm-sized Mn based ferrite was found to be 57.2–278.7 W/g under fields of 250–750 Oe, such values depend primarily on the applied field strength, frequency and particle size[51]. The combination of shape / morphology and magnetocrystalline anisotropies can lead to a complex dependence of these parameters on magnetic hyperthermia which may also depend on the specific material and crystalline structure[43,48,52–56].

Experimental

Synthesis of pure $MnFe_2O_4$ and GO-$MnFe_2O_4$ nanoparticles

$MnFe_2O_4$ nanoparticles were synthesized using 0.05 M Iron (III) Nitrate Nonahydrate (Aldrich, ≥ 98%) and 0.025 M Manganese (II) chloride tetra hydrate (Aldrich, 98%). Precursors were dissolved in 100 ml d. water and stirred for 30 min till the solution became clear. Then the pH of the previous mixture was adjusted to reach pH equal to 10 by adding NaOH (WINLAB, 98%) solution drop wise while stirring. After that, to get homogeneous solution, the mixture was stirred for another 15 min. The mixture was heated to 160 °C for 20 h with heating rate of 4 °C /min inside a Teflon lined stainless steel autoclave. The Teflon lined stainless was naturally cooled down to room temperature. Finally, the obtained powder was washed by using Centrifugation at 8000 rpm for 10 min with deionized waters, this washing procedure was repeated 3 times to get rid of the undispersed residue. The final washing was done using ethanol. Finally, the as obtained MNPs were dried at 80 °C in the oven. For the preparation of Go-$MnFe_2O_4$, GO (Aldrich) was added to 40 ml d. water and sonicated for at least for 40 min to get a dispersed solution. Other precursors, namely, Iron (III) Nitrate Nonahydrate and Manganese (II) chloride tetra hydrate were added to 60 ml d. water, with stirring for 30 min. Both solutions were mixed and stirred for another 30 min. Final thermal treatment was done as for the $MnFe_2O_4$. Case.

Synthesis of pure $CoFe_2O_4$and GO-$CoFe_2O_4$ nanoparticles

$CoFe_2O_4$ nanoparticles were synthesized using 1.4×10^{-2} M cobalt (II) chloride (Fluke, ≥ 98%) and 0. 2.8×10^{-2} M Iron acetyl acetonate (Aldrich, 97%). Precursors were dissolved in 100 ml di-water and stirred for 1 h. till the solution became clear. The pH of the previous mixture was adjusted to 11 by adding NaOH solution drop wise while stirring till homogenous solution is obtained. The mixture was heated to 220 °C for 15 h with heating rate 4 °C/min inside a Teflon lined stainless steel autoclave then cooled down to room temperature naturally. Finally, the obtained powder was washed, using d. water, several times by Centrifugation. The final washing was done using ethanol and the as obtained MNPs were dried at 80 °C in the oven. For the preparation of GO-$CoFe_2O_4$, GO (Aldrich) was added to 70 ml d. water and sonicated at least for 1 h to get a dispersed solution. Cobalt (II) chloride and Iron acetyl acetonate added to 30 ml di-water and stirred for 30 min. Both solutions were mixed and stirred for another 30 min hence other steps are similar as the above method.

Characterization of the nanoparticles

X-Ray powder diffraction analysis was carried out using a Panalytical X-ray diffractometer with Cu Kα target having radiation (λ = 1.5405 Å) for all samples. The crystallite size of nanoparticles was estimated from the peaks broadening using the well-known Scherer formula. Transmission electron microscope (TEM) images were taken using a JSM1400-PLUS-JEOL. Samples were prepared by placing a drop of the particles suspended in ethanol onto a carbon coated copper grid and allowing it to dry at room temperature. Particles distribution was obtained from TEM by manual measurement of the largest dimension along two perpendicular directions of more than 300 particles using ImageJ software. Vibrating sample magnetometer (VSM) (Quantum Design, 3T Versalab) was used to study magnetic properties. Feasibility for hyperthermia of 5 mg of the nanoparticles dispersed in 1 mL of water was measured using G2-D5 Series Multi-mode 1500 W Driver from Nanoscale Bio magnetics. The sample solution was placed into the G2-D5 coil, where the alternating magnetic field amplitude and frequency can be applied. The induced temperature of the solution was detected and recorded using a fiber-optic sensor. Raman spectra were measured at 532 nm by using a Confocal Raman microscope (WItec, 300R alpha, made in Germany) with Laser power 1mw. Fourier Transform Infrared (FT-IR) spectroscopy was conducted using a PerkinElmer Spectrum 2B (USA) spectrophotometer within the wavenumber range of 400–4000 cm^{-1} to analyse the structural features of PPACs nanocomposites, prepared in the form of potassium bromide (KBr) pellets. The Raman spectra and images presented in this work were recorded using a Confocal Raman Microscope (alpha 300 R from WITec GmbH, Ulm, Germany) equipped with a Nd-YAG laser working at 532 nm and an ultrahigh throughput spectrometer (UHTS 300) for Raman light analysis. FTIR spectra were recorded using (FT/IR-4600, JASCO Corp., Tokyo, Japan) FTIR spectrometer.

Results and discussion

Crystal structure and morphology

The XRD patterns of $MnFe_2O_4$, GO-$MnFe_2O_4$ and the standard $MnFe_2O_4$ pattern is shown in Fig. 1a. The peak positions and relative intensities match well with the standard XRD data for $MnFe_2O_4$ cubic spinel structure. The XRD pattern of $MnFe_2O_4$ exhibits diffraction peaks at 2θ = 18.09°, 29.78°, 35.08°, 36.68°, 42.6°, 52.77°, 56.3°, 61.8°, 73.06°, and 88.4°, corresponding to the (111), (220), (311), (222), (400), (422), (511), (440), (533), and (731) crystal planes of the spinel ferrite phase, respectively[57,58]. Attention was directed to the (311) reflection, as this peak is widely used as a diagnostic marker for lattice parameter variation, cation redistribution, and defect formation in spinel ferrites. The position of the (311) peak is highly sensitive to the occupancy of tetrahedral (A) and octahedral (B) sites by Mn^{2+} and Fe^{3+} ions, since ionic radii differences between these cations directly modulate the d-spacing of this reflection. The observed position at 2θ = 35.08° in bare $MnFe_2O_4$ is consistent with a partially inverse spinel configuration characteristic of hydrothermally synthesized $MnFe_2O_4$[57,58]. Upon incorporation into the GO composite, the (311) reflection shifts to 2θ = 35.73°, corresponding to a shift of + 0.65°.

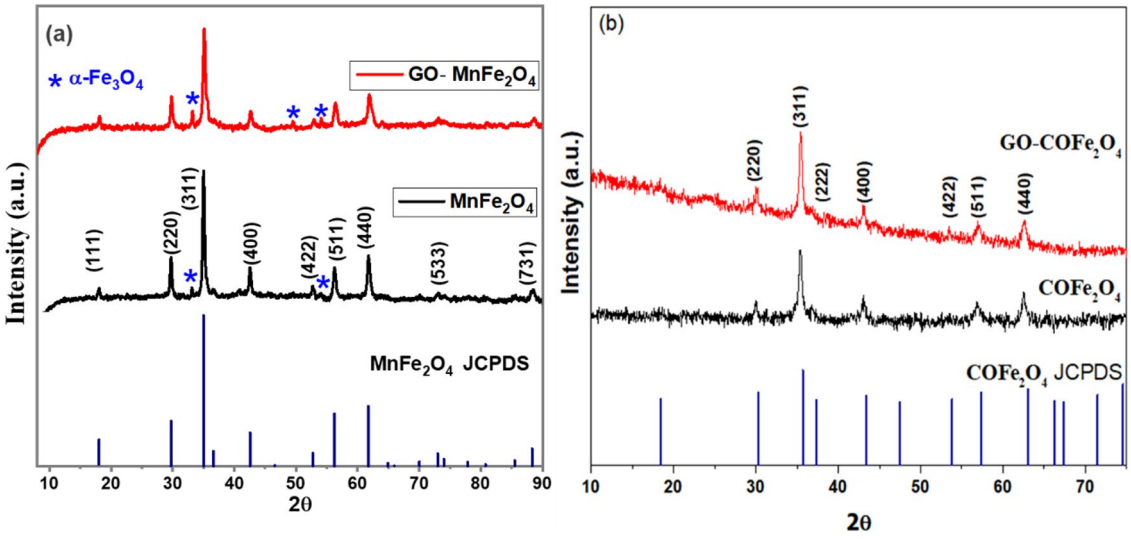


Fig. 1. X-ray diffraction pattern of (**a**) $MnFe_2O_4$, GO-$MnFe_2O_4$ nanocomposite and the standard for $MnFe_2O_4$ (**b**) $CoFe_2O_4$, GO-$CoFe_2O_4$ nanocomposites and the standard for $CoFe_2O_4$.

Using Bragg's law, this shift corresponds to a reduction in the (311) interplanar spacing from approximately 2.556 Å in bare $MnFe_2O_4$ to approximately 2.512 Å in the $MnFe_2O_4$-GO composite, representing a lattice contraction of roughly 1.7%. This contraction is indicative of compressive macrostrain introduced at the ferrite–graphene oxide interface, likely arising from electrostatic and coordinative interactions between surface metal cations and the oxygen-bearing functional groups of GO (hydroxyl, epoxide, and carboxyl groups). Such interfacial interactions can locally perturb the cation distribution near the nanoparticle surface, promoting partial migration of cations between A and B sites and thereby inducing measurable lattice distortion. Notably, minor peaks at 2θ = 33.07°, 49.5°, and 54.20° present in bare $MnFe_2O_4$ were indexed to the hematite phase (α-Fe_2O_3)[59,60], suggesting incomplete phase purity under the hydrothermal conditions used. Notably, when $MnFe_2O_4$ is combined with graphene oxide (GO) to form GO-$MnFe_2O_4$, the intensity of hematite peaks increased further which could be related to the presence of GO functional group. Those functional groups can interact with the iron precursors, altering the reaction pathway and leading to the presence of different iron oxide phases[61]. All XRD peaks in Fig. 1a are broad, indicating small crystalline size. The average crystallite size of both samples was calculated from the five most intense reflections using the Scherrer equation (Eq. 1) and was found to be 22.7 ± 2.8 nm and 18.5 ± 2.1 nm for $MnFe_2O_4$ and GO-$MnFe_2O_4$, respectively.

$$\boldsymbol{D} = \frac{0.93\,\boldsymbol{\lambda}}{\boldsymbol{\beta}\,\boldsymbol{\cos\theta}} \tag{1}$$

where D is the average crystallite size, λ is the X-ray wavelength (Cu-Kα, 1.5406 Å), β is the full width at half-maximum FWHM of the diffraction peak, and θ is the Bragg diffraction angle. While the Scherrer equation provides a convenient first-order estimate of crystallite size, it assumes that peak broadening arises solely from crystallite size effects and does not account for additional broadening contributions that are commonly present in nanostructured ferrites. Microstrain arising from lattice distortions, non-uniform cation distributions, and structural defects can contribute significantly to peak broadening and lead to an underestimation of true crystallite size if not corrected for. In the present system, the observed reduction in crystallite size from 22.7 ± 2.8 nm in bare $MnFe_2O_4$ to 18.5 ± 2.1 nm in GO-$MnFe_2O_4$ is consistent with the lattice contraction evidenced by the (311) peak shift discussed above, and likely reflects a combination of true crystallite size reduction and enhanced micro strain at the ferrite–GO interface. The oxygen-bearing functional groups of GO can interact with surface metal cations, introducing local lattice distortions that broaden diffraction peaks beyond what would be expected from size effects alone. Given the moderate number of well-resolved peaks available, the Scherrer values are reported as primary estimates with the aforementioned caveats acknowledged.

XRD patterns of the synthesized $CoFe_2O_4$ and GO-$CoFe_2O_4$ nanoparticles are shown in Fig. 1b. The observed diffraction peaks located at 2θ = 30.02°, 35.73°, 36.86°, 42.8°, 53.29°, 56.9°, and 62.54° are assigned to the (220), (311), (222), (400), (422), (511), and (440) planes of the $CoFe_2O_4$ phase, matching well with the standard single-phase spinel structure of $CoFe_2O_4$ (JCPDS no. 22-1086). The XRD patterns show that the characteristic peak of graphene oxide is not observable, indicating that GO incorporation does not significantly perturb the crystalline structure of $CoFe_2O_4$, consistent with the dominant diffraction signals of the spinel phase masking any residual GO reflection. The average crystallite size calculated from the FWHM using Eq. (1) was found to be 13.9 ± 1.5 nm and 14.7 ± 1.8 nm for $CoFe_2O_4$ and GO-$CoFe_2O_4$, respectively. Unlike the $MnFe_2O_4$ system, where GO incorporation produced a measurable reduction in crystallite size, the $CoFe_2O_4$ composite exhibits a marginal size increase of approximately 0.8 nm. This behavior may reflect the higher magnetic

anisotropy and greater lattice rigidity of $CoFe_2O_4$, which render its crystalline structure comparatively less susceptible to interfacial strain-induced size suppression. Nevertheless, the same caveats regarding Scherrer-based size estimation apply here: micro strain contributions from Co^{2+}/Fe^{3+} cation disorder across tetrahedral and octahedral sites, as well as instrumental broadening, may partially convolute the apparent crystallite size values reported for both $CoFe_2O_4$ and its GO composite. The close similarity between the two $CoFe_2O_4$ values further suggests that GO has a minimal effect on the crystallization behavior of the hard ferrite phase under the hydrothermal conditions employed.

Transmission electron microscope (TEM) images of both $MnFe_2O_4$ and GO-$MnFe_2O_4$ nanocrystals are shown in Fig. 2a,b, respectively. Figure 2a shows the well-defined $MnFe_2O_4$ particles which exhibit mixed morphology; cubic and/or cuboid with an edge length of around 14.9 nm and spheres (but to a lesser extent) (inset to Fig. 2a. The TEM images of GO-$MnFe_2O_4$ (Fig. 2b) show the formation of more spherical particles when compared to $MnFe_2O_4$. It can be clearly seen that two-dimensional GO nanosheets are exfoliated and $MnFe_2O_4$ nanoparticles are assembled on top of the sheets. Figure 2c,d show the corresponding histogram plots of the sizes using ImageJ analysis of both $MnFe_2O_4$ and GO-$MnFe_2O_4$, respectively. From the histogram, the calculated average particle size is 29.3 with standard deviation (SD) of ± 8 nm and 17.4 with SD of ± 4 nm for $MnFe_2O_4$ and GO-$MnFe_2O_4$, respectively. And as expected, particle size calculated from TEM is larger than those obtained from the XRD measurement. Morphology and particle size could significantly influence the material hyperthermia performance and SAR values[54].

Figure 3a,b show TEM for $CoFe_2O_4$ and GO-$CoFe_2O_4$, respectively. Both samples show spherical particles having average particle size of 13.5 with SD of ± 3.4 nm and 14.48 nm with SD of ± 3.8 nm, respectively. In the

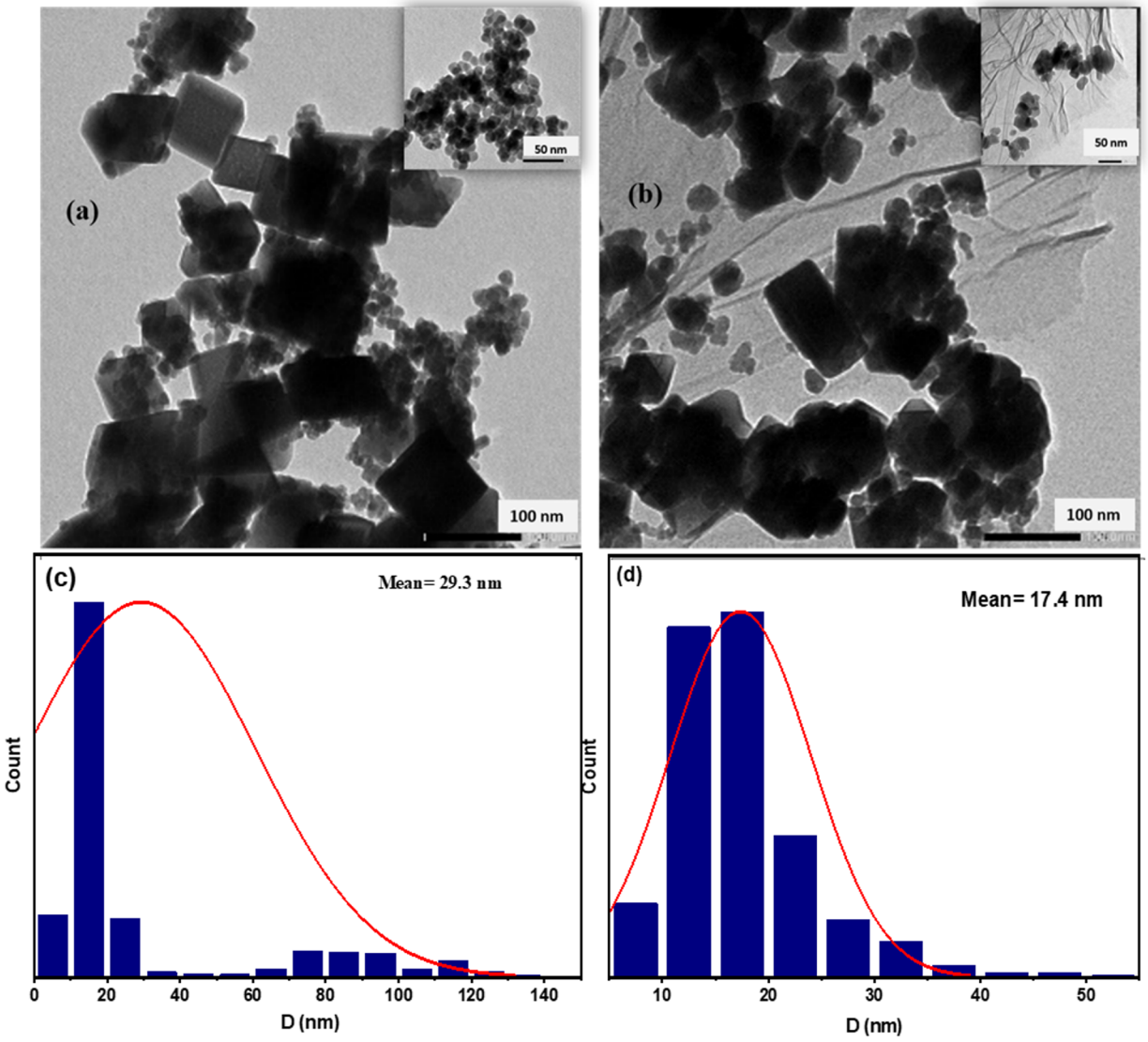


Fig. 2. TEM image for (**a**) $MnFe_2O_4$ (**b**) GO-$MnFe_2O_4$. The insets to fig. (**a**,**b**) show TEM image at lower magnification. Fig. (**c**,**d**) represents the size distribution for $MnFe_2O_4$ and GO-$MnFe_2O_4$ nanoparticles, respectively.

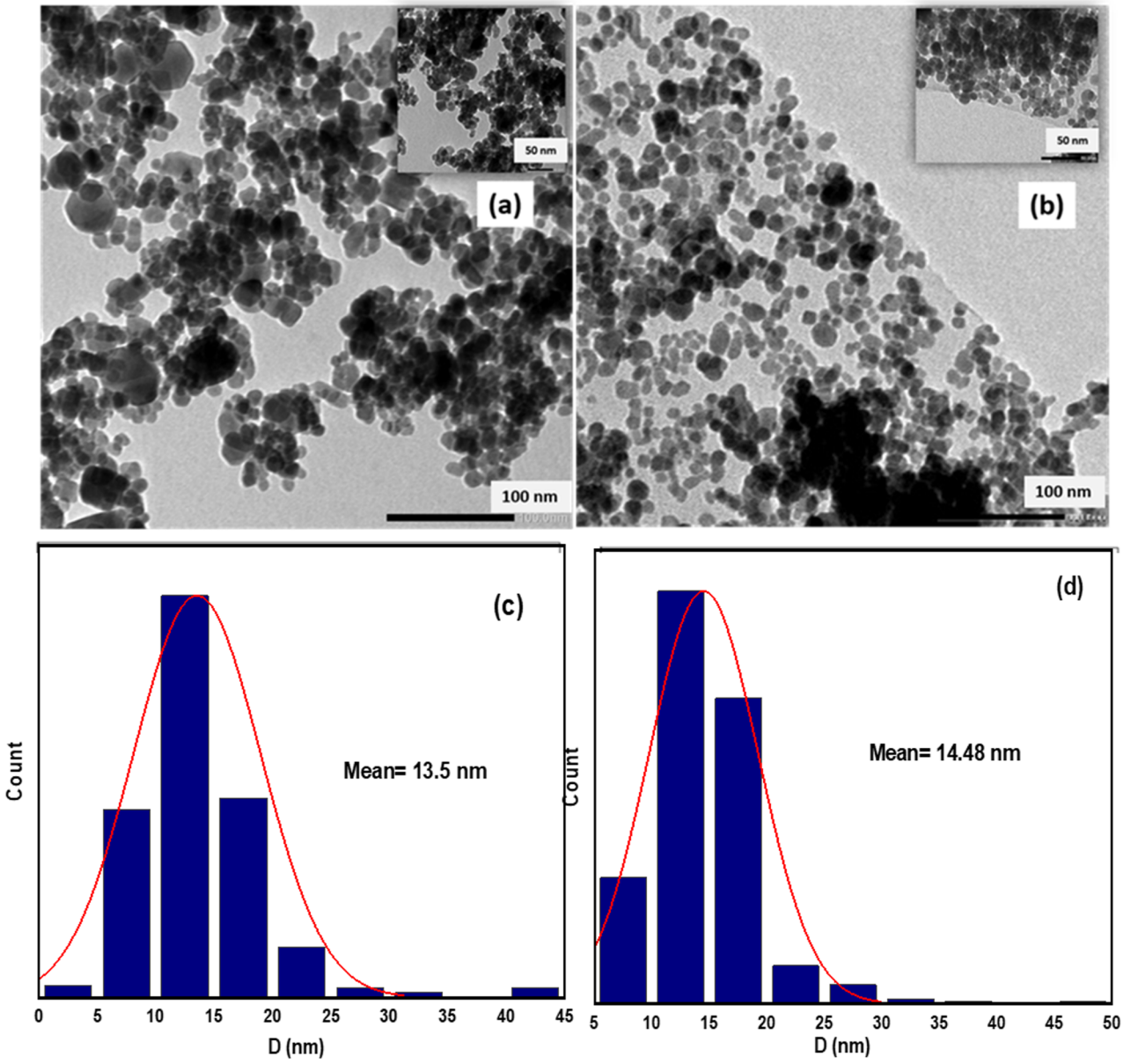


Fig. 3. TEM image for (**a**) $CoFe_2O_4$ (**b**) GO-$CoFe_2O_4$. The insets to fig. (**a**,**b**) show TEM image at lower magnification. Fig. (**c**,**d**) represents the size distribution for $CoFe_2O_4$ and GO-$CoFe_2O_4$ nanoparticles, respectively.

case of the GO-$CoFe_2O_4$ composite, particles were disbursed on the surface of the 2D GO sheets signifying a successful attachment of the ferrite nanoparticles on GO. Figure 3c,d show the corresponding histogram plots of $CoFe_2O_4$ and GO-$CoFe_2O_4$, respectively. One must mention here that the synthesis temperature and time used for $CoFe_2O_4$ were 220 °C and 15 h. respectively, which is different from those used in case of $MnFe_2O_4$, 160 °C and 20 h. The use of high temperature could truncate and smooth the particles edges, so a spherical shape is more likely to form in comparison to the synthesis at lower temperature[62]. On the other hand, the longer reaction time allows for the Ostwald ripening of the small particles, which are then dissolved and incorporated into the larger ones contributing to a broader size distribution[62–65]. In the case of $CoFe_2O_4$, when we used similar temperature and time to that of $MnFe_2O_4$, we observed a wide hysteresis loop with large value of coercive filed, H_c, which is not recommended for hyperthermia application.

Raman spectroscopy is a commonly used tool for the characterization of carbon products since conjugated and double carbon-carbon bonds lead to high Raman intensities. Figure 4a shows Raman spectra of GO, $MnFe_2O_4$ and GO-$MnFe_2O_4$. It shows the two fundamental bands of GO: D at 1347 cm^{-1} arising from the sp^3 carbon atoms of disordered graphite and G at 1588 cm^{-1} arising from sp^2- ordered graphite[66]. The I_D/I_G ratio was found to be 0.99. On the other hand, the active Raman bands observed at 636 cm^{-1}, 270, 210, 484 and 585 cm^{-1} are assigned to A_{g1}, E_g and $3T_{2g}$ of the $MnFe_2O_4$ structure respectively.[67]. Figure 4b shows Raman spectra of GO,

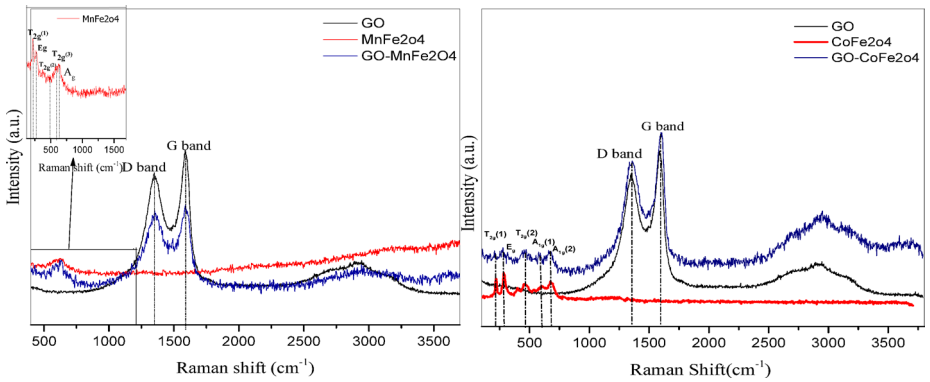


Fig. 4. Raman (**a**) for GO, GO-$MnFe_2O_4$ and $MnFe_2O_4$ and (**b**) for GO, GO-$CoFe_2O_4$ and $CoFe_2O_4$.

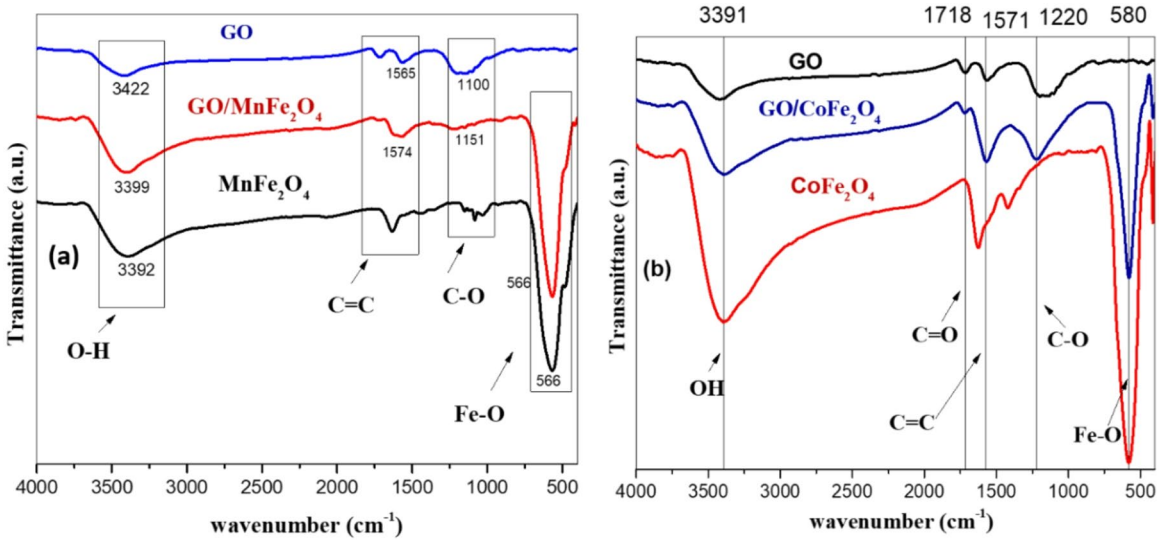


Fig. 5. FTIR spectra of (**a**) GO, GO-$MnFe_2O_4$ and $MnFe_2O_4$ (**b**) for GO, GO-$CoFe_2O_4$ and $CoFe_2O_4$.

$CoFe_2O_4$ and GO-$CoFe_2O_4$. As stated earlier in the case of Mn Ferrite and GO-Mn, two fundamental bands of GO: D at 1355 cm^{-1} and G at 1603 cm^{-1} and the I_D/I_G ratio was found to be 0.94. This calculated I_D/I_G value is slightly less than that of the GO-$MnFe_2O_4$ case, indicating presence of less defects. Bands at 668, 589, 454, 273 and 217 are assigned to A_{1g} (2), A_{1g} (1), T_{2g} (2) E_g and T_{2g} (1) for the $CoFe_2O_4$, respectively[68,69]. Raman results verify the successful synthesis of the $MnFe_2O_4$, $CoFe_2O_4$ and the structural constancy of graphene oxide in the composites. In Raman spectroscopy the I_D/I_G ratio measures the structural disorder and the density of defects/oxygen functional groups in the graphene lattice. In this context, the lower I_D/I_G ratio for GO- $CoFe_2O_4$ composite compared to that of GO- $MnFe_2O_4$ indicates that the former has fewer defects, lower functional group density as well as a higher degree of graphitization. This is consistent with the XRD results, which show no reflections from impurity phases or defects in the cobalt composite, unlike the GO-$MnFe_2O_4$ composite, which contains the impurity phase hematite.

FTIR spectroscopy was used to investigate the effect of graphene oxide on ferrites NPS and to verify the integrity of the NPS. Figure 5a shows FTIR for $MnFe_2O_4$, GO-$MnFe_2O_4$ and GO for the purpose of comparison. It clearly indicates the formation of GO- $MnFe_2O_4$ composite. It's observed a broad peak from (3392 cm^{-1}-3422 cm^{-1} which is a fingerprint of Hydroxyl group stretching vibrations of adsorbed water. FTIR of GO-$MnFe_2O_4$ shows the vibrations of functional groups C=C Aromatic group and C–O epoxy group at 1574 and 1151, respectively[70]. In addition to the absorption peak at 566 cm^{-1} which represent the Fe–O stretching vibration in tetrahedral sites that only present in the spectra of $MnFe_2O_4$ and GO-$MnFe_2O_4$[71,72]. Figure 5b shows FTIR for $CoFe_2O_4$, obtained in the presence of graphene oxide. According to FTIR spectra exhibited a broad peak at approximately 3391 cm^{-1} which corresponds to the -OH Hydroxyl group, 1718 cm^{-1} C=O as a fingerprint for carboxyl group,1571 cm^{-1} which corresponds to C=C as Aromatic group and 1220 cm^{-1} which corresponds to C–O epoxy group[73]. In addition to the cobalt ferrite peak is observed at 580 cm^{-1} which represent the Fe–O stretching vibration in tetrahedral sites[71,72]. From the above mentioned FTIR spectroscopy, one can clearly identify abundant oxygen-containing functional groups on the surface of GO sheets like carboxyl, hydroxyl and epoxy groups, which make the surface of GO negatively charged. When GO suspension was poured into the

metal cations (Mn and Co) solution, they are adsorbed on the surface of GO nanosheets through electrostatic attractions.

Magnetic properties and hyperthermia measurements

$CoFe_2O_4$ and $MnFe_2O_4$ are both ferrimagnetic compounds but exhibit distinctly different magnetic behavior: $MnFe_2O_4$ is classified as a "soft ferrite" while $CoFe_2O_4$ is classified as a "hard ferrite," a distinction that arises primarily from the different inversion degrees characterizing each spinel structure[74]. The magnetocrystalline anisotropy constant (K_1) of $CoFe_2O_4$ is reported in the range of $2.0–3.0 \times 10^5$ J/m^3, whereas $MnFe_2O_4$ exhibits a much lower K_1 of approximately -0.36×10^5 J/m^3 [75], reflecting the dominant role of Co^{2+} ions occupying octahedral sites in generating strong uniaxial anisotropy. One cannot ignore the surface and finite size effects that are known to play a key role in the magnetic properties of nanoparticles[76,77]. A direct correlation between magnetization and particle size has been reported in several ferrite systems[48,53,54], making it important to establish this effect for the present composites.

The room-temperature M×H loops of the standalone Co and Mn ferrites and their GO composites were measured and are shown in Fig. 6a–c. For $MnFe_2O_4$ and GO-$MnFe_2O_4$ nanoparticles, nearly zero remanence magnetization is observed at 300 K, confirming superparamagnetic behavior at room temperature. The measured saturation magnetization (M_S) values of 60 emu/g and 50 emu/g, and coercive fields of HC ≈ 65 Oe and ≈ 50 Oe for $MnFe_2O_4$ and GO-$MnFe_2O_4$, respectively (Fig. 6a, are consistent with values reported in the literature for hydrothermally synthesized $MnFe_2O_4$ nanoparticles of comparable size. Specifically, M_S values in the range of 38–64 emu/g and H_C values below 100 Oe have been widely reported for hydrothermally synthesized $MnFe_2O_4$ nanoparticles in the 15–30 nm size range[78,79], confirming that our samples fall within the expected magnetic parameter space for this system. The M_S value of 60 emu/g obtained here is notably lower than the bulk value of 82 emu/g[80], a reduction of approximately 27%, This reduction is consistent with the well-established surface spin canting effect in which the noncollinear arrangement of magnetic spins at the nanoparticle surface creates a magnetically disordered shell that does not contribute to the net magnetization[81]. The further reduction to 50 emu/g upon GO incorporation (a decrease of ~ 17% relative to bare $MnFe_2O_4$) is in line with reports on similar ferrite–GO and ferrite–carbon matrix composites, where the nonmagnetic matrix dilutes the magnetic phase and introduces additional surface disorder through interfacial metal–oxygen interactions[82,83].

The hysteresis loops of $CoFe_2O_4$ and GO-$CoFe_2O_4$ nanoparticles (Fig. 6c) exhibit the characteristic features of hard ferromagnetic materials. The measured coercivity values of H_C ≈ 2.5 kOe and ≈ 2.0 kOe, and MS values of ≈ 40 emu/g and ≈ 35 emu/g for $CoFe_2O_4$ and GO-$CoFe_2O_4$, respectively. These values are in good agreement with literature reports for $CoFe_2O_4$ nanoparticles in the 10–20 nm size range synthesized by hydrothermal methods, where H_C values of 1.5–3.0 kOe and M_S values of 35–55 emu/g are commonly reported[84,85]. The measured M_S of 40 emu/g represents a reduction of 50% relative to the bulk value of 80 emu/g[86], a larger relative reduction than observed for $MnFe_2O_4$ (27%). This more pronounced suppression of magnetization in $CoFe_2O_4$ nanoparticles is consistent with their higher surface anisotropy and greater sensitivity to surface spin disorder, which is amplified in high-anisotropy systems where canted surface spins are more strongly pinned and thus more effectively excluded from contributing to the net moment[87]. The coercivity of 2.5 kOe observed for our $CoFe_2O_4$ sample is within the broad range reported for this system (0.5–5.0 kOe), with the specific value reflecting a combination of particle size, synthesis conditions, and degree of cation inversion[84]. The reduction in H_C from 2.5 kOe to 2.0 kOe upon GO incorporation is attributed to surface anisotropy dilution caused by the non-magnetic GO matrix interfering with the coherent spin reversal mechanism, an effect also reported by Venkatesha et al. for $CoFe_2O_4$–graphene oxide composites[82]. As expected, the M_S values of both ferrite systems are significantly lower than their respective bulk counterparts, as bulk $CoFe_2O_4$ and $MnFe_2O_4$ exhibit M_S values of 80 emu/g[86] and 82 emu/g[80], respectively. The reduction in magnetization with decreasing particle size is a well-documented consequence of increased surface-to-volume ratio: as particle size decreases, the proportion of surface spins exhibiting canted or disordered configurations increases, leading to a net reduction in magnetization[81]. Since GO is nonmagnetic, it contributes negatively or not at all to the overall magnetization, further lowering M_S in the composite samples.

Figure 6b,d show the zero-field-cooled (ZFC) and field-cooled (FC) magnetization as a function of temperature at a constant applied field of 200 Oe. The ZFC/FC bifurcation and the peak in the ZFC curve define the blocking temperature (T_B), which marks the transition between the superparamagnetic (fast relaxation) and blocked (slow relaxation) regimes. T_B values of 310 K and 330 K were obtained for $MnFe_2O_4$ and GO-$MnFe_2O_4$, respectively. The slight increase in T_B upon GO incorporation is consistent with enhanced interparticle dipolar interactions mediated by the GO matrix. Such interaction can restrict nanoparticle moment relaxation and effectively raise the energy barrier for spin reversal, an effect well established in nanoparticle–matrix systems where reduced inter-particle spacing or physical confinement strengthens dipolar coupling. The T_B values near room temperature for the $MnFe_2O_4$ system are in good agreement with reported values for $MnFe_2O_4$ nanoparticles of similar size[78,79], and are consistent with the superparamagnetic behavior evidenced by the near-zero coercivity observed in the room-temperature hysteresis loops. For $CoFe_2O_4$ and GO-$CoFe_2O_4$, T_B > 400 K, well above room temperature, consistent with the high magnetocrystalline anisotropy of $CoFe_2O_4$ that stabilizes magnetic domains against thermal fluctuations up to elevated temperatures.

This is in agreement with the literature, where T_B values exceeding 400 K are routinely reported for $CoFe_2O_4$ nanoparticles even at sizes below 20 nm[79,80], reflecting the dominant role of anisotropy energy over thermal energy in this system. Figure 7a shows the temperature increase as a function of time for both ferrites and their GO composites suspended in water at a concentration of 5 mg/mL under an alternating magnetic field of 300 Oe (23.9 kA/m) and frequency of 304 kHz. All samples can generate heat under these conditions. $MnFe_2O_4$ shows a significantly greater temperature increase compared to the GO-$MnFe_2O_4$ composite, which is attributed to the reduced magnetization of the composite upon GO incorporation. In the case of $CoFe_2O_4$ and GO-$CoFe_2O_4$, a smaller temperature increase is observed in both cases with approximately the same shape of the heating

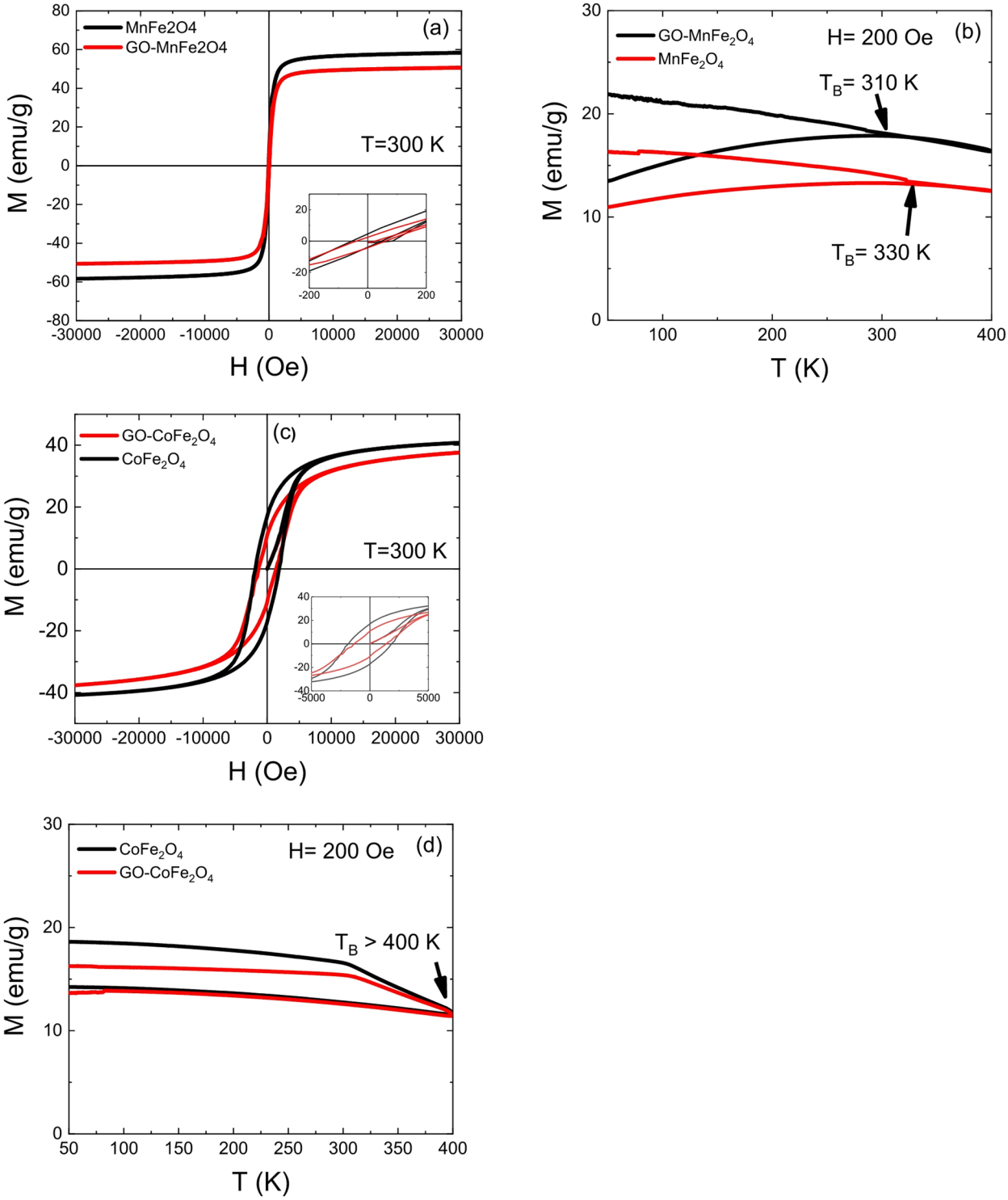


Fig. 6. (**a**,**c**) magnetic hysteresis loops of ferrite system at 300 k for GO-$MnFe_2O_4$, $MnFe_2O_4$ and GO-$CoFe_2O_4$, $CoFe_2O_4$, respectively. (**b**,**d**) ZFC-FC magnetization curves taken under 200 Oe for GO-$MnFe_2O_4$, $MnFe_2O_4$ and GO-$CoFe_2O_4$, $CoFe_2O_4$, respectively.

curves. These results can be understood in terms of the distinct magnetic properties of the two ferrite systems, and particularly the role of magnetic anisotropy in determining which relaxation mechanism dominates heat dissipation under the experimental field conditions applied here. The magnetocrystalline anisotropy constant K_{eff} is 3.3×10^3 J/m^3 for $MnFe_2O_4$ and 2.7×10^5 J/m^3 for $CoFe_2O_4$[88], a difference of nearly two orders of magnitude, and this contrast is central to understanding the divergent hyperthermia behavior of the two systems. The induced heating mechanism arises from energy dissipation by magnetic nanoparticles under an

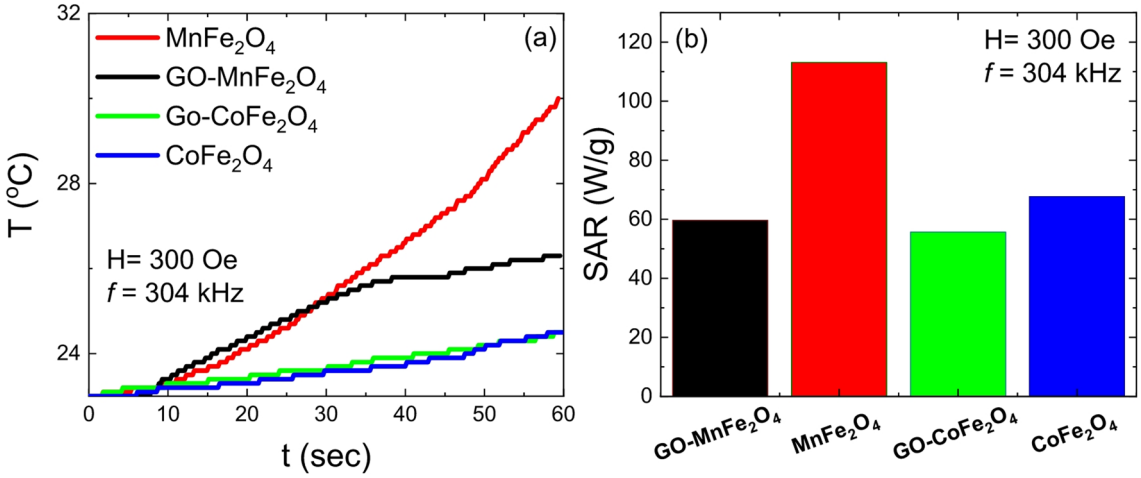


Fig. 7. (**a**) Hyperthermia temperature curves for GO-$MnFe_2O_4$, $MnFe_2O_4$, GO-$CoFe_2O_4$ and $CoFe_2O_4$ in concentration of 5 mg/mL in water under field application of 300 Oe and 304 kHz (**b**) Calculated specific absorption rate (SAR) from initial slope of T × t curve for GO-$MnFe_2O_4$, $MnFe_2O_4$, GO-$CoFe_2O_4$ and $CoFe_2O_4$ nanoparticles.

alternating magnetic field (AMF), and two major relaxation pathways contribute to this dissipation. The first is Néel relaxation, in which the internal magnetization rotates between easy axes within a magnetically blocked particle without physical rotation of the particle itself. The Néel relaxation time is given by

$$\tau_N = \tau_0 \exp\left(\frac{KV}{k_B T}\right)$$

where $\tau_o \sim 10^{-10}$ s is the characteristic attempt time, K is the anisotropy constant, V is the particle volume, k_B is the Boltzmann constant, and T is the absolute temperature. The argument of the exponential, KV/k_BT, is the ratio of the anisotropy energy barrier to thermal energy and is the decisive parameter governing whether Néel relaxation is efficient under a given AMF frequency. The second is Brownian relaxation, in which the entire nanoparticle physically rotates within the carrier fluid, dragging its magnetic moment with it. The Brownian relaxation time is $\tau_B = \frac{3\eta V_h}{k_B T}$, where η is the dynamic viscosity of the carrier fluid and V_h is the hydrodynamic volume of the nanoparticle. Brownian relaxation is independent of the anisotropy constant K and depends instead on particle size and the viscous properties of the medium. In a real suspension, the effective relaxation time τ_{eff} is given by the harmonic mean of the two contributions $\frac{1}{\tau_{eff}} = \frac{1}{\tau_N} + \frac{1}{\tau_B}$.

Maximum heating efficiency is achieved when $\tau_{eff} \approx 1/(2\pi f)$, i.e., when the effective relaxation time is matched to the period of the applied AMF. At the experimental frequency of 304 kHz, the optimal relaxation time is approximately $\tau_{opt} \approx 5.2 \times 10^{-7}$ s. For $MnFe_2O_4$, with $K = 3.3 \times 10^3$ J/m^3 and a crystallite size of approximately 24 nm ($V \approx 7.24 \times 10^{-24}$ m^3), the Néel energy barrier KV/k_BT at room temperature (T = 300 K) is approximately

$$\frac{KV}{k_B T} = \frac{3.3 \times 10^3 \times 7.24 \times 10^{-24}}{1.38 \times 10^{-23} \times 300} \approx 5.77$$

giving a Néel relaxation time of $\tau_N \approx \tau_{0_o} \exp(5.77) \approx 3.2 \times 10^{-8}$ s. This value is short relative to the AMF period ($\tau_{opt} \approx 5.2 \times 10^{-7}$ s), indicating that the magnetization of $MnFe_2O_4$ can follow the AMF with relatively low lag, and that Néel relaxation is fast and efficient. Under the aqueous suspension conditions of this experiment ($\eta_{water} \approx 8.9 \times 10^{-4}$ Pa s), the Brownian relaxation time for a particle with a hydrodynamic diameter of ~ 30 nm (accounting for a hydration shell) is $\tau_B \approx 3 \times 8.9 \times 10^{-4} \times (\pi/6)(30 \times 10^{-5})^3/(1.38 \times 10^{-23} \times 300) \approx 3.8 \times 10^{-5}$ s. Since τ_N and τ_B are of similar magnitude for $MnFe_2O_4$, both Néel and Brownian mechanisms operate concurrently, with τ_{eff} falling in the range $1–2 \times 10^{-5}$ s. While this is still somewhat shorter than τ_{opt}, the low-anisotropy character of $MnFe_2O_4$ means the energy barrier per cycle is modest, allowing the magnetization to respond rapidly and efficiently to the oscillating field, resulting in appreciable hysteretic losses per cycle and the higher SAR values observed. For $CoFe_2O_4$, with $K = 2.7 \times 10^5$ J/m^3 and a crystallite size of approximately 13.9 nm ($V \approx 1.40 \times 10^{-24}$ m^3), the Néel energy barrier is

$$\frac{KV}{k_B T} = \frac{2.7 \times 10^5 \times 1.40 \times 10^{-24}}{1.38 \times 10^{-23} \times 300} \approx 91.3$$

giving $\tau_N \approx 10^{-10} \times \exp(91.3) \approx 10^{-10} \times 10^{39.7}$ s, an astronomically large value that is many orders of magnitude beyond any physically accessible timescale. This result has a critical implication: Néel relaxation is completely frozen out in $CoFe_2O_4$ at room temperature under these field conditions. The anisotropy barrier is so large that

internal magnetization reversal cannot occur within the AMF period, and the particle behaves as a magnetically blocked, single-domain particle. This is consistent with the conventional hard-magnetic hysteresis loop observed in Fig. 6c and the $T_B > 400$ K measured from ZFC/FC curves. Since Néel relaxation does not contribute to heating in $CoFe_2O_{44}$, Brownian relaxation is the only active heating mechanism in this system. However, because $\tau_{eff} \approx \tau_B \approx 10^{-8}$ s for particles of this size in water, which is still significantly shorter than $\tau_{opt} \approx 5.2 \times 10^{-7}$ s, the Brownian mechanism also operates sub-optimally, leading to reduced energy absorption per cycle and consequently lower SAR values relative to $MnFe_2O_4$. The near-identical heating curves of $CoFe_2O_4$ and GO-$CoFe_2O_4$ further support this interpretation: since heating in this system arises entirely from viscous (Brownian) rotation rather than internal magnetization dynamics, the nonmagnetic GO matrix, which does not significantly alter the particle's hydrodynamic volume or the suspension viscosity at this loading, has a comparatively minor effect on τ_B and hence on SAR, explaining why the two $CoFe_2O_4$-based samples show similar temperature rise profiles.

In this light, the superior SAR of $MnFe_2O_4$ (110 W/g) relative to $CoFe_2O_4$ (70 W/g) under the experimental conditions used here is a direct consequence of the anisotropy-mediated relaxation dynamics: $MnFe_2O_4$ benefits from concurrent Néel and Brownian contributions with relaxation times that are better matched to the applied frequency, while $CoFe_2O_4$ is limited to Brownian relaxation alone with its internal magnetization effectively locked along the easy axis. This analysis also clarifies why the two systems respond differently to GO incorporation. In the low-anisotropy $MnFe_2O_4$ system, where Néel relaxation contributes substantially, the introduction of GO reduces M_S and introduces domain-pinning defects (oxygen vacancies and residual α-Fe_2O_3 phase as evidenced from XRD), directly impairing the internal magnetization dynamics and causing a ~ 45% reduction in SAR (from 110 to 60 W/g). In contrast, in $CoFe_2O_4$ where only Brownian relaxation is operative, the GO matrix has minimal influence on τ_B at the concentrations studied, and the SAR changes only marginally from 70 to 60 W/g. From the initial slope of the T vs. t curves shown in Fig. 7a, SAR values were calculated for all four samples and are presented in Fig. 7b. SAR = 110 W/g for $MnFe_2O_4$, 60 W/g for GO-$MnFe_2O_4$, 70 W/g for $CoFe_2O_4$, and 60 W/g for GO-$CoFe_2O_4$. The significant decrease in SAR upon GO incorporation into $MnFe_{22}O_4$ is attributable to the combined effects of: (i) dilution of the magnetic phase by the nonmagnetic GO matrix, reducing the effective M_S per gram of composite; (ii) introduction of structural defects including oxygen vacancies and the impurity α-Fe_2O_3 phase (as identified by XRD), which generate non-isotropic strain and pin magnetic domains, preventing them from responding freely to the AMF; and (iii) interfacial interactions between the ferrite surface and GO functional groups that perturb cation distribution and locally suppress the magnetization, as discussed in the XRD and magnetic sections above. Beyond the anisotropy and relaxation mechanism arguments, the calculated SAR values are also influenced by particle size, morphology, and surface anisotropy. The surface anisotropy contribution, which increases with decreasing particle size due to the growing surface-to-volume ratio, is particularly relevant here. In the framework of Néel's surface anisotropy model, surface symmetry breaking, arising from structural defects, multifaceted surfaces, broken exchange bonds, coordination number reduction, and surface strain, contributes an additional effective anisotropy term that augments the bulk magnetocrystalline value[89]. The distinct morphologies observed for the two ferrite systems are therefore relevant: $MnFe_2O_4$ exhibits a cubic/cuboid morphology with well-defined facets, while $CoFe_2O_4$ presents a more spherical morphology. Faceted surfaces, as in the cuboid case, offer flat crystallographic planes with relatively ordered surface spin configurations, whereas the nominally spherical $CoFe_2O_4$ particles, which in practice exhibit irregular multi-faceted surfaces at the nanoscale, present more surface disorder[63]. Despite spin canting existing in both systems due to their small particle sizes, the greater surface disorder in the spherical $CoFe_2O_4$ nanoparticles is expected to further enhance the effective surface anisotropy, adding to the already large magnetocrystalline K value and further deepening the Néel relaxation freeze-out in this system. This morphology-dependent surface anisotropy effect thus reinforces the conclusion that $CoFe_2O_4$ operates exclusively in the Brownian relaxation regime under the field and frequency conditions of this study. Meanwhile, $MnFe_2O_4$ benefits from a more thermally accessible combined relaxation mechanism that underpins its superior heating performance. Note: The numerical estimates for τ_N and τ_B are derived from the particle sizes and anisotropy constants stated in the manuscript.

By comparing our results to literature (Table 1) and (Table 2), we found that SAR values reported in this work are higher than or comparable to many of the published works under same conditions of particle size, magnetization and AMF parameters. Samples showing higher SAR values are either caped with some biocompatible materials, having larger particle size, and/or AMF parameters like field strength and frequency are higher than those values adopted in the current work, 300 Oe and 304 kHz.

Conclusion

This study presents a systematic investigation of $MnFe_2O_4$ and $CoFe_2O_4$ nanoparticles and their graphene oxide composites synthesized via a hydrothermal approach, with the aim of elucidating the relationship between magnetic anisotropy, relaxation dynamics, and hyperthermia performance. The central finding is that magnetic anisotropy is the primary determinant of heating efficiency under the experimental AMF conditions (300 Oe, 304 kHz): the low-anisotropy $MnFe_2O_4$ system ($K = 3.3 \times 10^3$ J/m^3) benefits from concurrent Néel and Brownian relaxation mechanisms whose effective relaxation time is better matched to the applied frequency, yielding a SAR of 110 W/g. In contrast, the high-anisotropy $CoFe_2O_4$ system ($K = 2.7 \times 10^5$ J/m^3) operates exclusively through Brownian relaxation, as its Néel relaxation is thermally inaccessible under these conditions, resulting in a substantially lower SAR of 70 W/g. These results demonstrate that maximizing SAR in ferrite-based hyperthermia agents requires not only high saturation magnetization but careful tuning of the anisotropy constant to match the relaxation timescale to the applied field frequency, a design principle that is clearly illustrated by the contrasting behavior of the soft and hard ferrite systems studied here. The incorporation of graphene oxide introduced competing effects: while it improved colloidal dispersion and offers a surface platform amenable to

No.	Sample	M_s(emu/g)	SAR (W/g)	f (kHz)	H (Oe)	D (nm)	Ref.
1	$MnFe_2O_4$	67	356.17	265	335.2	13	[90]
2	$MnFe_2O_4$	–	295	195	628.3	20	[91]
3	$MnFe_2O_4$	58.8	148.4	1950	56.54	19	[44]
4	$MnFe_2O_4/SiO_2$	-	336	400	320	18	[92]
5	$PVP/MnFe_2O_4$	60	468.37	265	335.2	13	[93]
6	Mn@silica	40	84.65	260	69.11	14	[94]
8	$MnFe_2O_4$@Chitosan	-	320	342	200	15	[95]
9	$MnFe_2O_4$	56.4	145.78	316	295	9	[96]
10	$MnFe_2O_4$ $GO/MnFe_2O_4$	50 10	90	310	300	17	[97]
			170	310	700		
			80	310	300		
			280	310	800		
12	$MnFe_2O_4$ $GO/ MnFe_2O_4$	60 50	110	304	300	14.89 15.5	This work
			60	304	300		

Table 1. Comparison of our data with the list of published similar work of $MnFe_2O_4$.

No.	Sample	MS (emu/g)	SAR (W/g)	Freq. (kHz)	Field (Oe)	D (nm)	Ref.
1	$GO/ CoFe_2O_4$	40	2 mg 77.4 1 mg 232.5	200 150	300	5	[98]
2	$CoFe_2O_4$@OA/OLA	70	297	450	300	6–20	[99]
3	Aminodextran/ $CoFe_2O_4$	50	259 518	327 981	170 230	10–50	[100]
4	$CoFe_2O_4$	63	133	101	510	28	[101]
5	CA- $CoFe_2O_4$	43	76	329	1201	4 to 7	[102]
6	$CoFe_2O_4$	55.3	9.6	85	80	7.2	[103]
7	$CoFe_2O_4$	63	29	300	188	6	[104]
8	$CoFe_2O_4$	60	99	420	187	8.9	[105]
9	$CoFe_2O_4$	71	185.32	316	295	10	[106]
10	$CoFe_2O_4$	80	248	350	440	9.45	[107]
11	$CoFe_2O_4$	39	142	178	80	13	[108]
12	$GO/CoFe_2O_4$ $CoFe_2O_4$	40 35	70 60	304 304	300 300	12.5 14	This work

Table 2. Comparison of our data with the list of published similar work of $CoFe_2O_4$.

bioconjugation and functionalization for targeted drug delivery, it consistently reduced SAR values across both ferrite systems. In $MnFe_2O_4$-GO, the SAR reduction from 110 to 60 W/g is attributed to magnetic phase dilution by the nonmagnetic GO matrix, domain pinning by interfacial strain and structural defects, and the suppression of hematite impurity phases that, while removing a non-contributing secondary phase, also reflects broader perturbations to the magnetic microstructure at the ferrite–GO interface. In $CoFe_2O_4$-GO, the marginal SAR change from 70 to 60 W/g is consistent with the Brownian-dominated mechanism in this system being relatively insensitive to the internal magnetic modifications introduced by GO. Taken together, these findings establish that the trade-off between the dispersibility benefits and the SAR penalties of GO incorporation is system-dependent and must be evaluated in the context of the dominant relaxation mechanism. From a materials design perspective, this work identifies $MnFe_2O_4$ as the more promising candidate for magnetic hyperthermia among the systems studied, owing to its favorable combination of magnetization, anisotropy, and relaxation dynamics at clinically relevant field conditions. The particle size (~ 23 nm), morphology, and surface anisotropy contributions further modulate its performance and offer clear handles for optimization. Future work should focus on systematic variation of particle size and GO loading to map the full SAR parameter space, surface functionalization of the composites with targeting ligands for tumor-specific delivery, and evaluation of heating performance in viscous and gel-like media that more closely approximate the intratumoral environment, where Brownian relaxation is suppressed and Néel relaxation becomes the exclusive heating pathway, a condition under which the anisotropy contrast between $MnFe_2O_4$ and $CoFe_2O_4$ would be expected to become even more pronounced. Ultimately, in vitro cytotoxicity assays and in vivo hyperthermia efficacy studies are essential next steps toward translating these findings into clinically viable therapeutic platforms.

Data availability

The datasets generated and/or analysed during the current study are available from the corresponding author on reasonable request.

Received: 14 February 2026; Accepted: 27 April 2026
Published online: 12 May 2026

References

1. Patade, S. R. et al. Preparation and characterisations of magnetic nanofluid of zinc ferrite for hyperthermia. *Nanomater. Energy*. **9**, 8–13 (2020).
2. Westra, A. & Dewey, W. Variation in sensitivity to heat shock during the cell-cycle of Chinese hamster cells in vitro. *Int. J. Radiat. Biol. Relat. Stud. Phys. Chem. Med.* **19**, 467–477 (1971).
3. Rao, W. & Deng, Z. S. A review of hyperthermia combined with radiotherapy/chemotherapy on malignant tumors. *Crit. Rev. Biomed. Eng.* **38** (2010).
4. Mehdaoui, B. et al. Optimal size of nanoparticles for magnetic hyperthermia: a combined theoretical and experimental study. *Adv. Funct. Mater.* **21**, 4573–4581 (2011).
5. Huang, X., Jain, P. K., El-Sayed, I. H. & El-Sayed, M. A. Plasmonic photothermal therapy (PPTT) using gold nanoparticles. *Lasers Med. Sci.* **23**, 217–228 (2008).
6. Hirsch, L. R. et al. Nanoshell-mediated near-infrared thermal therapy of tumors under magnetic resonance guidance. *Proc. Natl. Acad. Sci.* **100**, 13549–13554 (2003).
7. Huang, N. et al. Single-wall carbon nanotubes assisted photothermal cancer therapy: Animal study with a murine model of squamous cell carcinoma. *Lasers Surg. Med.* **42**, 798–808 (2010).
8. Burke, A. et al. Long-term survival following a single treatment of kidney tumors with multiwalled carbon nanotubes and near-infrared radiation. *Proc. Natl. Acad. Sci.* **106**, 12897–12902 (2009).
9. Zhou, J. et al. NIR photothermal therapy using polyaniline nanoparticles. *Biomaterials* **34**, 9584–9592 (2013).
10. Ramadan, W. et al. Substrate-induced strain effects on the transport properties of pulsed laser-deposited Nb-doped SrTiO3 films. *Appl. Phys. Lett.* **88** (2006).
11. Ramadan, W. et al. Room temperature rectifying characteristics of epitaxial Y1Ba2Cu3 – xZnxO7 – δ (x = 0.0, 0.2) and Nb: SrTiO3 (Nb: 0.05%, 0.1%, 0.5%) heterojunctions. *J. Appl. Phys.* **99** (2006).
12. Ramadan, A. & Ramadan, W. Superior performance of asymmetric supercapacitor based on Cu doped bismuth ferrite electrode. *J. Energy Storage*. **100**, 113702. https://doi.org/10.1016/j.est.2024.113702 (2024).
13. Ramadan, W., Dillert, R., Koch, J., Tegenkamp, C. & Bahnemann, D. W. Changes in the solid-state properties of bismuth iron oxide during the photocatalytic reformation of formic acid. *Catal. Today*. **326**, 22–29. https://doi.org/10.1016/j.cattod.2018.09.003 (2019).
14. Fu, L. et al. Interface and defect structures in YBa2Cu3O7 – δ and Nb: SrTiO3 heterojunction. *J. Phys. D.* **40**, 187 (2006).
15. Lee, J. H. et al. Exchange-coupled magnetic nanoparticles for efficient heat induction. *Nat. Nanotechnol.* **6**, 418–422 (2011).
16. Fantechi, E. et al. A smart platform for hyperthermia application in cancer treatment: cobalt-doped ferrite nanoparticles mineralized in human ferritin cages. *ACS Nano*. **8**, 4705–4719 (2014).
17. Le Renard, P. E. et al. The in vivo performance of magnetic particle-loaded injectable, in situ gelling, carriers for the delivery of local hyperthermia. *Biomaterials* **31**, 691–705 (2010).
18. Hergt, R. et al. Physical limits of hyperthermia using magnetite fine particles. *IEEE Trans. Magn.* **34**, 3745–3754 (1998).
19. Rosensweig, R. E. Heating magnetic fluid with alternating magnetic field. *J. Magn. Magn. Mater.* **252**, 370–374 (2002).
20. Niculaes, D. et al. Asymmetric assembling of iron oxide nanocubes for improving magnetic hyperthermia performance. *ACS Nano*. **11**, 12121–12133 (2017).
21. Nandwana, V. et al. Exchange coupling in soft magnetic nanostructures and its direct effect on their theranostic properties. *ACS Appl. Mater. Interfaces*. **10**, 27233–27243 (2018).
22. Hergt, R. & Dutz, S. Magnetic particle hyperthermia—biophysical limitations of a visionary tumour therapy. *J. Magn. Magn. Mater.* **311**, 187–192 (2007).
23. Silva, A. C. et al. Application of hyperthermia induced by superparamagnetic iron oxide nanoparticles in glioma treatment. *Int. J. Nanomed.* **6**, 591–603. https://doi.org/10.2147/IJN.S14737 (2011).
24. Maier-Hauff, K. et al. Efficacy and safety of intratumoral thermotherapy using magnetic iron-oxide nanoparticles combined with external beam radiotherapy on patients with recurrent glioblastoma multiforme. *J. Neurooncol.* **103**, 317–324. https://doi.org/10.1007/s11060-010-0389-0 (2011).
25. Brezovich, I. A. Low frequency hyperthermia: capacitive and ferromagnetic thermoseed methods. *Med. Phys. Monogr.* **16**, 82–111 (1988).
26. Wust, P. et al. Magnetic nanoparticles for interstitial thermotherapy–feasibility, tolerance and achieved temperatures. *Int. J. Hyperth.* **22**, 673–685 (2006).
27. Ganure, K. A., Dhale, L. A., Shirsat, S. E. & Lohar, K. S. Morphological study of lanthanum-doped nano spinel ferrite via normal micelles method. *J. Inorg. Organomet. Polym Mater.* **28**, 1821–1828. https://doi.org/10.1007/s10904-018-0825-8 (2018).
28. Hatamie, S. et al. *Colloids Surf. B* **146**, 271–279 (2016).
29. Hassani, A. et al. Heterogeneous sono-Fenton-like process using magnetic cobalt ferrite-reduced graphene oxide (CoFe2O4-rGO) nanocomposite for the removal of organic dyes from aqueous solution. *Ultrason. Sonochem.* **40**, 841–852 (2018).
30. Ganure, K. A. et al. Synthesis, structural and magnetic properties of Ni2 + and In3 + doped cobalt ferrite and application as catalyst for synthesis of Bis-(Indolyl) methane derivatives. *Mater. Today Proc.* **47**, 1747–1754. https://doi.org/10.1016/j.matpr.2021.02.327 (2021).
31. Khan, M. A. et al. Optimized inductive heating of a superparamagnetic ZnxMn1–xFe2O4 hydrophilic magneto-viscoelastic fluid for hyperthermia application. *ACS Appl. Biol. Mater.* **8**, 11003–11018. https://doi.org/10.1021/acsabm.5c01685 (2025).
32. Singh, A. et al. Tailored nanoparticles for magnetic hyperthermia: Highly stable aqueous dispersion of Mn-substituted magnetite superparamagnetic nanoparticles by double surfactant coating for improved heating efficiency. *J. Alloys Compd.* **976**, 172999. https://doi.org/10.1016/j.jallcom.2023.172999 (2024).
33. Katoch, G. et al. Harnessing magnesium ferrite for sustainable Malachite Green dye degradation: insights into photocatalytic mechanisms, material design, and wastewater remediation. *Environ. Sci. Europe*. **38**, 35. https://doi.org/10.1186/s12302-025-01298-0 (2026).
34. Katoch, G. et al. Impact of Cu and La on the structural, morphological, magnetic, photocatalytic, and antibacterial traits of cobalt spinel nanoferrites. *Ionics* **30**, 5093–5110. https://doi.org/10.1007/s11581-024-05619-w (2024).
35. Ganure, K., Tiwari, S., Bhosle, S., Kamble, N. & Singh, A. Eco-friendly synthesis of pyrimidine derivatives using a magnetically recoverable and reusable catalyst. *J. Inorg. Organomet. Polym. Mater.* **35**, 8788–8800. https://doi.org/10.1007/s10904-025-03820-6 (2025).

36. Ganure, K. A., Langade, M. M., Dhale, L. A. & Lohar, K. S. Chromium substituted nickel ferrites (NiFe2 – xCrxO4, x = 0.0, 0.1, 0.2, 0.3, and 0.4) magnetically recoverable reusable heterogeneous nano catalysts. *Mater. Today: Proc.* **46**, 6139–6144. https://doi.org/10.1016/j.matpr.2020.04.029 (2021).
37. Zeleňáková, A. et al. Cobalt-ferrite nano-cubes for magnetic hyperthermia applications. *J. Alloys Compd.* **989**, 174415. https://doi.org/10.1016/j.jallcom.2024.174415 (2024).
38. Jhala, I. G. et al. Structural and magnetic properties of cobalt ferrite nanoparticles synthesized by auto–combustion sol–gel method. *Next Mater.* **9**, 101120. https://doi.org/10.1016/j.nxmate.2025.101120 (2025).
39. Lima, A. C. et al. Evaluation of (BH)max and magnetic anisotropy of cobalt ferrite nanoparticles synthesized in gelatin. *Ceram. Int.* **41**, 11804–11809. https://doi.org/10.1016/j.ceramint.2015.05.148 (2015).
40. Zeng, X. et al. Direct observation of cation distributions of ideal inverse spinel CoFe2O4 nanofibres and correlated magnetic properties. *Nanoscale* **9**, 7493–7500. https://doi.org/10.1039/C7NR02013A (2017).
41. Sanpo, N. et al. Biocompatibility of transition metal-substituted cobalt ferrite nanoparticles. *J. Nanopart. Res.* **16**, 2510. https://doi.org/10.1007/s11051-014-2510-3 (2014).
42. Pandhare, A. B. et al. Chitosan-functionalized lithium iron oxide nanoparticles for magnetic hyperthermia applications. *Langmuir* **40**, 25902–25918. https://doi.org/10.1021/acs.langmuir.4c03228 (2024).
43. Gasser, A. et al. Feasibility of superparamagnetic NiFe2O4 and GO-NiFe2O4 nanoparticles for magnetic hyperthermia. *Mater. Sci. Eng. B.* **297**, 116721. https://doi.org/10.1016/j.mseb.2023.116721 (2023).
44. Doaga, A. et al. Synthesis and characterizations of manganese ferrites for hyperthermia applications. *Mater. Chem. Phys.* **143**, 305–310 (2013).
45. Vamvakidis, K. et al. Reducing the inversion degree of MnFe 2 O 4 nanoparticles through synthesis to enhance magnetization: evaluation of their 1 H NMR relaxation and heating efficiency. *Dalton Trans.* **43**, 12754–12765 (2014).
46. Topkaya, R., Kurtan, U., Baykal, A. & Toprak, M. S. Polyvinylpyrrolidone (PVP)/MnFe2O4 nanocomposite: Sol–Gel autocombustion synthesis and its magnetic characterization. *Ceram. Int.* **39**, 5651–5658 (2013).
47. Mendo, S. G. et al. Hyperthermia studies of ferrite nanoparticles synthesized in the presence of cotton. *New J. Chem.* **39**, 7182–7193 (2015).
48. Thirupathi, G. & Singh, R. Magneto-viscosity of MnZn-ferrite ferrofluid. *Phys. B Condens. Matter*. **448**, 346–348. https://doi.org/10.1016/j.physb.2014.03.042 (2014).
49. Xu, C. & Sun, S. New forms of superparamagnetic nanoparticles for biomedical applications. *Adv. Drug Deliv. Rev.* **65**, 732–743 (2013).
50. Astefanoaei, I., Gimaev, R., Zverev, V., Tishin, A. & Stancu, A. Cubic and sphere magnetic nanoparticles for magnetic hyperthermia therapy: Computational results. *Nanomaterials* **13**, 2383 (2023).
51. Patel, H. & Parekh, K. Synthesis and characterization of octahedron and cube shape Mn0.5Zn0.5Fe2O4 particle dispersion for magnetic fluid hyperthermia. *Ceram. Int.* **50**, 44852–44864. https://doi.org/10.1016/j.ceramint.2024.08.321 (2024).
52. Getahun, Y., Das, D., Ramana, C. V. & El-Gendy, A. A. Nanoengineered pure Fe in a citrate matrix (Fe–CIT) with significant and tunable magnetic properties. *Nanotechnology* **35**, 48LT01. https://doi.org/10.1088/1361-6528/ad6fa5 (2024).
53. Elabbasi, M. & El-Gendy, A. A. In-vitro evaluation of in-situ synthesized superparamagnetic iron nanoparticles (SPINs) for magnetic hyperthermia treatment of breast and prostate cancer. *Biomed. Mater.* **20**, 045016. https://doi.org/10.1088/1748-605X/addf27 (2025).
54. Mohapatra, J. et al. Enhancing the magnetic and inductive heating properties of Fe3O4 nanoparticles via morphology control. *Nanotechnology* **31**, 275706 (2020).
55. Beg, M. S., Mohapatra, J., Pradhan, L., Patkar, D. & Bahadur, D. Porous Fe3O4-SiO2 core-shell nanorods as high-performance MRI contrast agent and drug delivery vehicle. *J. Magn. Magn. Mater.* **428**, 340–347 (2017).
56. Getahun, Y. et al. Superparamagnetic iron oxide nanoparticles functionalized by biocompatible ligands with enhanced high specific absorption rate for magnetic hyperthermia. *Colloids Surf. A*. **693**, 134036. https://doi.org/10.1016/j.colsurfa.2024.134036 (2024).
57. Ueda Yamaguchi, N., Bergamasco, R. & Hamoudi, S. Magnetic MnFe2O4–graphene hybrid composite for efficient removal of glyphosate from water. *Chem. Eng. J.* **295**, 391–402. https://doi.org/10.1016/j.cej.2016.03.051 (2016).
58. Ghobadi, M., Gharabaghi, M., Abdollahi, H., Boroumand, Z. & Moradian, M. MnFe2O4-graphene oxide magnetic nanoparticles as a high-performance adsorbent for rare earth elements: Synthesis, isotherms, kinetics, thermodynamics and desorption. *J. Hazard. Mater.* **351**, 308–316. https://doi.org/10.1016/j.jhazmat.2018.03.011 (2018).
59. Gandha, K. et al. Mesoporous iron oxide nanowires: Synthesis, magnetic and photocatalytic properties. *RSC Adv.* **6**, 90537–90546. https://doi.org/10.1039/C6RA18530D (2016).
60. Chernyshova, I. V., Hochella Jr, M. F. & Madden, A. S. Size-dependent structural transformations of hematite nanoparticles. 1. Phase transition. *Phys. Chem. Chem. Phys.* **9**, 1736–1750. https://doi.org/10.1039/B618790K (2007).
61. Tang, H., Gao, P., Xing, A., Tian, S. & Bao, Z. One-pot low-temperature synthesis of a MnFe 2 O 4–graphene composite for lithium ion battery applications. *RSC Adv.* **4**, 28421–28425 (2014).
62. Salazar-Alvarez, G. et al. Cubic versus spherical magnetic nanoparticles: The role of surface anisotropy. *J. Am. Chem. Soc.* **130**, 13234–13239 (2008).
63. Lifshitz, I. M. & Slyozov, V. V. The kinetics of precipitation from supersaturated solid solutions. *J. Phys. Chem. Solids*. **19**, 35–50 (1961).
64. Wagner, C. Theorie der alterung von niederschlägen durch umlösen (Ostwald-reifung). *Z. für Elektrochemie Berichte der Bunsengesellschaft für Phys. Chemie*. **65**, 581–591 (1961).
65. Kale, G. et al. Annealing-induced defect modulation and functional switching in ZnO thin films: DFT and molecular docking analysis. *J. Inorg. Organomet. Polym. Mater.* https://doi.org/10.1007/s10904-025-04163-y (2026).
66. Song, P., Zhang, X., Sun, M., Cui, X. & Lin, Y. Synthesis of graphene nanosheets via oxalic acid-induced chemical reduction of exfoliated graphite oxide. *RSC Adv.* **2**, 1168–1173 (2012).
67. Gasparov, L. et al. Infrared and Raman studies of the Verwey transition in magnetite. *Phys. Rev. B.* **62**, 7939 (2000).
68. Chandramohan, P., Srinivasan, M., Velmurugan, S. & Narasimhan, S. Cation distribution and particle size effect on Raman spectrum of CoFe2O4. *J. Solid State Chem.* **184**, 89–96 (2011).
69. Alazmi, A. et al. Cobalt ferrite supported on reduced graphene oxide as a T 2 contrast agent for magnetic resonance imaging. *RSC Adv.* **9**, 6299–6309 (2019).
70. Cui, H. J., Shi, J. W., Yuan, B. & Fu, M. L. Synthesis of porous magnetic ferrite nanowires containing Mn and their application in water treatment. *J. Mater. Chem. A*. **1**, 5902–5907 (2013).
71. Wei, W., Cui, X., Chen, W. & Ivey, D. G. Manganese oxide-based materials as electrochemical supercapacitor electrodes. *Chem. Soc. Rev.* **40**, 1697–1721. https://doi.org/10.1039/C0CS00127A (2011).
72. Sahoo, B., Sahu, S. K., Nayak, S., Dhara, D. & Pramanik, P. Fabrication of magnetic mesoporous manganese ferrite nanocomposites as efficient catalyst for degradation of dye pollutants. *Catal. Sci. Technol.* **2**, 1367–1374. https://doi.org/10.1039/C2CY20026K (2012).
73. Tayyebi, A. & Outokesh, M. Supercritical synthesis of a magnetite-reduced graphene oxide hybrid with enhanced adsorption properties toward cobalt & strontium ions. *RSC Adv.* **6**, 13898–13913 (2016).
74. Cruz, M. M. et al. Enhanced magnetic hyperthermia of CoFe2O4 and MnFe2O4 nanoparticles. *J. Alloys Compd.* **703**, 370–380. https://doi.org/10.1016/j.jallcom.2017.01.297 (2017).

75. Sato, R. et al. Precise control of the emission wavelength on perovskite quantum dots by crystal lattice shrinkage/expansion of the A site mixture. *ACS Appl. Opt. Mater.* **2**, 2031–2038. https://doi.org/10.1021/acsaom.4c00266 (2024).
76. Coey, J. M. D. Noncollinear spin arrangement in ultrafine ferrimagnetic crystallites. *Phys. Rev. Lett.* **27**, 1140–1142. https://doi.org/10.1103/PhysRevLett.27.1140 (1971).
77. Martínez, B. et al. Magnetic properties of γ-Fe2O3 nanoparticles obtained by vaporization condensation in a solar furnace. *J. Appl. Phys.* **79**, 2580–2586. https://doi.org/10.1063/1.361125 (1996).
78. Gao, J., Auchmann, B., Hug, C., Pautz, A. & Sanfilippo, S. Study of a current-based quench detection method for CCT magnets via a co-wound superconducting sensing wire. *IEEE Trans. Appl. Supercond.* **31**, 1–5. https://doi.org/10.1109/TASC.2021.3059602 (2021).
79. Salih, S. J. & Mahmood, W. M. Review on magnetic spinel ferrite (MFe < sub>2 O<sub > 4) nanoparticles: From synthesis to application</sub >. *Heliyon* **9** https://doi.org/10.1016/j.heliyon.2023.e16601 (2023).
80. Aslibeiki, B., Kameli, P. & Ehsani, M. H. MnFe2O4 bulk, nanoparticles and film: A comparative study of structural and magnetic properties. *Ceram. Int.* **42**, 12789–12795. https://doi.org/10.1016/j.ceramint.2016.05.041 (2016).
81. Kalaiselvan, C. R. et al. Manganese ferrite (MnFe2O4) nanostructures for cancer theranostics. *Coord. Chem. Rev.* **473**, 214809. https://doi.org/10.1016/j.ccr.2022.214809 (2022).
82. Venkatesha, N. et al. Ultrafine graphene oxide–CoFe2O4 nanoparticle composite as T1 and T2 contrast agent for magnetic resonance imaging. *RSC Adv.* **6**, 17423–17429. https://doi.org/10.1039/C5RA27186J (2016).
83. Seal, P., Paul, N., Babu, P. D. & Borah, J. P. Hyperthermic efficacy of suitably functionalized MWCNT decorated with MnFe2O4 nanocomposite. *Appl. Phys. A.* **125**, 290. https://doi.org/10.1007/s00339-019-2589-6 (2019).
84. Nguyen, A. T. & Kim, H. K. Visible-light-mediated synthesis of oxime esters via multicomponent reactions of aldehydes, aryl amines, and N-hydroxyphthalimide esters. *RSC Adv.* **13**, 31346–31352. https://doi.org/10.1039/D3RA06737H (2023).
85. Babić-Stojić, B. et al. Magnetic and structural studies of CoFe2O4 nanoparticles suspended in an organic liquid. *J. Nanomater.* **2013**, 741036. https://doi.org/10.1155/2013/741036 (2013).
86. Karaagac, O., Yildiz, B. B. & Köçkar, H. The influence of synthesis parameters on one-step synthesized superparamagnetic cobalt ferrite nanoparticles with high saturation magnetization. *J. Magn. Magn. Mater.* **473**, 262–267. https://doi.org/10.1016/j.jmmm.2018.10.063 (2019).
87. Pianciola, B. N. et al. Size and surface effects in the magnetic order of CoFe2O4 nanoparticles. *J. Magn. Magn. Mater.* **377**, 44–51. https://doi.org/10.1016/j.jmmm.2014.10.054 (2015).
88. Sellmyer, D. & Skomski, R. *Advanced Magnetic Nanostructures* (Springer, 2006).
89. Salazar-Alvarez, G. et al. Cubic versus spherical magnetic nanoparticles: The role of surface anisotropy. *J. Am. Chem. Soc.* **130**, 13234–13239. https://doi.org/10.1021/ja0768744 (2008).
90. Ghutepatil, P. & Pawar, S. Structural, morphological, magnetic and self-heating studies of one-step polyol synthesized manganese ferrite (MnFe2O4) nanoparticles. *Int. J. Nanosci.* **19**, 1950003 (2020).
91. ÇE, D. D., Manna, P. K., Nickel, R., Aktürk, S. & van Lierop, J. Comparative heating efficiency of cobalt-, manganese-, and nickel-ferrite nanoparticles for a hyperthermia agent in biomedicines. *ACS Appl. Mater. Interfaces.* **11**, 6858–6866 (2019).
92. Qiu, Q. W., Xu, X. W., He, M. & Zhang, H. W. Radio-frequency-heating capability of silica-coated manganese ferrite nanoparticles. *Chin. Phys. B.* **24**, 067503 (2015).
93. Ghutepatil, P., Khot, V. M. & Salunkhe, A. B. Design of monodispersed PVP functionalized biocompatible manganese ferrite nanoparticles for hyperthermia application. *Mater. Today: Proc.* **62**, 5341–5346 (2022).
94. Iqbal, Y., Bae, H., Rhee, I. & Hong, S. Magnetic heating of silica-coated manganese ferrite nanoparticles. *J. Magn. Magn. Mater.* **409**, 80–86 (2016).
95. Islam, K. et al. Manganese ferrite nanoparticles (MnFe2O4): Size dependence for hyperthermia and negative/positive contrast enhancement in MRI. *Nanomaterials* **10**, 2297 (2020).
96. Manohar, A., Krishnamoorthi, C., Pavithra, C. & Thota, N. Magnetic hyperthermia and photocatalytic properties of MnFe 2 O 4 nanoparticles synthesized by solvothermal reflux method. *J. Supercond. Novel Magn.* **34**, 251–259 (2021).
97. Le, A. T. et al. Enhanced magnetic anisotropy and heating efficiency in multi-functional manganese ferrite/graphene oxide nanostructures. *Nanotechnology* **27**, 155707 (2016).
98. Hatamie, S. et al. Hyperthermia of breast cancer tumor using graphene oxide-cobalt ferrite magnetic nanoparticles in mice. *J. Drug Deliv. Sci. Technol.* **65**, 102680 (2021).
99. Nam, P. H. et al. Polymer-coated cobalt ferrite nanoparticles: Synthesis, characterization, and toxicity for hyperthermia applications. *New J. Chem.* **42**, 14530–14541 (2018).
100. Khizar, S. et al. Aminodextran coated CoFe2O4 nanoparticles for combined magnetic resonance imaging and hyperthermia. *Nanomaterials* **10**, 2182 (2020).
101. Mazario, E. et al. Magnetic hyperthermia properties of electrosynthesized cobalt ferrite nanoparticles. *J. Phys. Chem. C.* **117**, 11405–11411 (2013).
102. Munjal, S., Khare, N., Sivakumar, B. & Sakthikumar, D. N. Citric acid coated CoFe2O4 nanoparticles transformed through rapid mechanochemical ligand exchange for efficient magnetic hyperthermia applications. *J. Magn. Magn. Mater.* **477**, 388–395 (2019).
103. Lavorato, G. et al. Bifunctional CoFe2O4/ZnO core/shell nanoparticles for magnetic fluid hyperthermia with controlled optical response. *J. Phys. Chem. C.* **122**, 3047–3057 (2018).
104. Cruz, M. et al. Enhanced magnetic hyperthermia of CoFe2O4 and MnFe2O4 nanoparticles. *J. Alloys Compd.* **703**, 370–380 (2017).
105. De Santana, W. M. O. et al. Ureasil–polyether–CoFe2O4 nanocomposites: Coupling a drug delivery system and magnetic hyperthermia. *ACS Appl. Polym. Mater.* **3**, 4837–4848 (2021).
106. Manohar, A., Geleta, D. D., Krishnamoorthi, C. & Lee, J. Synthesis, characterization and magnetic hyperthermia properties of nearly monodisperse CoFe2O4 nanoparticles. *Ceram. Int.* **46**, 28035–28041 (2020).
107. Kharat, P. B., Somvanshi, S. B., Khirade, P. P. & Jadhav, K. Induction heating analysis of surface-functionalized nanoscale CoFe2O4 for magnetic fluid hyperthermia toward noninvasive cancer treatment. *ACS Omega.* **5**, 23378–23384 (2020).
108. Munjal, S., Khare, N., Sivakumar, B. & Nair Sakthikumar, D. Citric acid coated CoFe2O4 nanoparticles transformed through rapid mechanochemical ligand exchange for efficient magnetic hyperthermia applications. *J. Magn. Magn. Mater.* **477**, 388–395. https://doi.org/10.1016/j.jmmm.2018.09.007 (2019).

Author contributions

W.R. provided research directions, discussed the data analysis and results with authors, edited and revised the manuscript. A.G. performed experiments including the synthesis and the characterization of physical properties for the samples, analyzed the data and wrote the initial report of the data under supervision of W.R. and A.A.E. A.R. helped A.G. in the synthesis experiments and data analysis. MG and YG performed the phase structure, magnetic and hyperthermia measurements, analyzed the data and discussed the result with A.A.E. A.A.E. designed the idea and experiments, provided research directions, discussed the results with the authors, edited, and revised the manuscript.

Funding
Open access funding provided by The Science, Technology & Innovation Funding Authority (STDF) in cooperation with The Egyptian Knowledge Bank (EKB).

Declarations

Competing interests
The authors declare no competing interests.

Additional information
Correspondence and requests for materials should be addressed to W.R. or A.A.E.-G.

Reprints and permissions information is available at www.nature.com/reprints.

Publisher's note Springer Nature remains neutral with regard to jurisdictional claims in published maps and institutional affiliations.

Open Access This article is licensed under a Creative Commons Attribution 4.0 International License, which permits use, sharing, adaptation, distribution and reproduction in any medium or format, as long as you give appropriate credit to the original author(s) and the source, provide a link to the Creative Commons licence, and indicate if changes were made. The images or other third party material in this article are included in the article's Creative Commons licence, unless indicated otherwise in a credit line to the material. If material is not included in the article's Creative Commons licence and your intended use is not permitted by statutory regulation or exceeds the permitted use, you will need to obtain permission directly from the copyright holder. To view a copy of this licence, visit http://creativecommons.org/licenses/by/4.0/.

© The Author(s) 2026